Supplemental Material for "Orbit-Transfer Torque Driven Field-Free Switching of Perpendicular Magnetization"

Xing-Guo Ye (叶兴国)†, Peng-Fei Zhu（朱鹏飞）†, Wen-Zheng Xu(徐文正)†, Nianze Shang(尚念泽), Kaihui Liu(刘开辉), and Zhi-Min Liao(廖志敏)*

State Key Laboratory for Mesoscopic Physics and Frontiers Science Center for Nano-optoelectronics, School of Physics, Peking University; Beijing 100871, China.

*Corresponding author. Email: liaozm@pku.edu.cn

†These authors contributed equally to this work.

Device Fabrication

Few layer WTe_2 was obtained from high-quality artificially grown crystals of bulk WTe_2 commercially purchased from HQ Graphene through standard mechanically exfoliated method. Few layer Fe_3GeTe_2 was obtained in a similar way. Then we patterned Ti/Au electrodes (~10 nm thick) onto an individual SiO_2/Si substrate with a circular disc configuration through e-beam lithography, metal deposition and lift-off. To achieve a better contact, the electrodes were precleaned by air plasma. Exfoliated BN flake (~20 nm thick), few layer Fe_3GeTe_2 (~10-15 nm thick) and few layer WTe_2 (~2-15 nm thick) were sequentially picked up and then transferred onto the Ti/Au electrodes using a polymer-based dry transfer technique[1]. The whole exfoliated and transfer processes were done in an argon-filled glove box with O_2 and H_2O content below 0.01 parts per million to avoid sample degradation.

Polarized Raman spectroscopy of few-layer WTe_2

The Raman spectroscopy was measured with 514 nm excitation wavelengths through a linearly polarized solid-state laser beam. The polarization of the excitation laser was controlled by a half-wave plate and a polarizer. The Raman scattered light with the same polarization as the excitation laser were collected. As shown in Fig. S2b, five Raman peaks are observed, which belong to the A1 modes of WTe_2 (Ref. [2]). The polarization dependence of intensities of peaks P2 and P11 (denoted in Fig. S2b) are presented in Figs. S2c and S2d, respectively. Based on previous reports[2], the polarization direction with maximum intensity was assigned as the *b* axis. The determined crystalline axes, i.e., *a* axis and *b* axis, are further denoted by the black arrows in the optical image (Fig. S2a).

Transport Measurements

All transport measurements were carried out in an Oxford cryostat with a variable temperature insert and a superconducting magnet. First-, second- and third-harmonic voltage signals were collected by standard lock-in techniques (Stanford Research Systems Model SR830) with frequency ω = 17.777 Hz unless otherwise stated. A sequence of pulse-like d.c. current I_P was applied through a Keithley 2400 SourceMeter. I_P was swept in steps of 0.2 mA. After every I_P was applied and then removed, the Hall resistance was measured as applying a 0.1 mA bias a.c. current.

Basic Transport Properties of Device A

The resistivity ρ_{xx} of device A along *a* axis as a function of temperature was measured, as shown in Fig. S3a. By considering a parallel resistance model, we could obtain the resistivity of

WTe_2 by $\rho_{xx}^{WTe_2} = {t_{WTe_2}}\big/{(\frac{t}{\rho_{xx}} - \frac{t_{FGT}}{\rho_{xx}^{FGT}})}$, where $\rho_{xx}^{WTe_2}$ is the resistivity of WTe_2, ρ_{xx}^{FGT} is the resistivity of Fe_3GeTe_2, t_{WTe_2} is the thickness of WTe_2, t_{FGT} is the thickness of Fe_3GeTe_2 and $t = t_{WTe_2} + t_{FGT}$. Referring to the $\rho_{xx}^{FGT}(T)$ previously reported by Z. Fei *et al* (Ref. [54]), the $\rho_{xx}^{WTe_2}$ was calculated and presented in Fig. S3a. Furthermore, the fraction of current flowing in the WTe_2 layer is estimated by $\frac{I_{WTe_2}}{I} = \frac{1}{1+\frac{\rho_{xx}^{WTe_2}}{\rho_{xx}^{FGT}}\frac{t_{FGT}}{t_{WTe_2}}}$, where I is the applied current flowing in the whole heterostructure, and I_{WTe_2} is the current component flowing in the WTe_2 layer. For other angles, $\rho_{xx}^{WTe_2}$ was estimated through the intrinsic resistivity anisotropy of WTe_2 following $\rho_{xx}(\theta) = \rho_a sin^2(\theta - \theta_0) + \rho_b cos^2(\theta - \theta_0)$, where ρ_a and ρ_b are resistivity along a axis and b axis, respectively, θ_0 corresponds to b axis.

The magneto-transport properties of device A at 1.8 K are shown in Fig. S3b. The large non-saturated magnetoresistance and Hall resistance demonstrate two-carrier transport characteristics, indicating a nearly compensated electron and hole density in WTe_2. Through a semi-classical two-carrier model[4], that is, $\rho_{xx} = \frac{1}{e}\frac{n\mu_n + p\mu_p + (n\mu_p + p\mu_n)\mu_n\mu_p B^2}{(n\mu_n + p\mu_p)^2 + (n-p)^2\mu_n^2\mu_p^2 B^2}$ and $\rho_{xy} = \frac{1}{e}\frac{(p\mu_p^2 - n\mu_n^2)B + (p-n)\mu_n^2\mu_p^2 B^3}{(n\mu_n + p\mu_p)^2 + (n-p)^2\mu_n^2\mu_p^2 B^2}$, where n is the electron density, p is the hole density, μ_n is the electron mobility and μ_p is the hole mobility, the carrier density and mobility are estimated as, $n = 1.51 \times 10^{13}\ cm^{-2}$, $p = 0.99 \times 10^{13}\ cm^{-2}$, $\mu_n = 2203\ cm^2/V \cdot s$ and $\mu_p = 1497\ cm^2/V \cdot s$.

Higher-order Hall effect in WTe_2

Due to the nonzero Berry curvature dipole on the surface, second-order nonlinear Hall effect is expected in few-layer WTe_2 (Ref.[34]). By utilizing the disc geometry of the electrodes, angle-dependence of the second-order nonlinear Hall effect was investigated, as shown in Fig. 2, which could help to confirm the alignment between electrodes and crystalline axis of WTe_2. Based on the symmetry of WTe_2, the second-order nonlinear Hall effect shows angle-dependence following $\frac{V_H^{2\omega}}{(I^\omega)^2} \propto sin(\theta - \theta_0)[d_{12}r^2 sin^2(\theta - \theta_0) + (d_{11} - 2d_{26}r^2)cos^2(\theta - \theta_0)]$ (Ref.[30]), where $V_H^{2\omega}$ is the second-harmonic Hall voltage, I^ω is the applied a.c. current, r is the resistance anisotropy, d_{ij} are the elements of the second-order nonlinear susceptibility tensor for the *Pm* point group, θ_0 is the angle misalignment between $\theta = 0°$ and crystalline b axis. The fitting curve for this angle dependence is shown by the red line in Fig. 2d, which yields the misalignment θ_0 equals 1.3° in device A.

In addition to the second-order nonlinear Hall effect, it is recently also reported a third-order nonlinear Hall effect in the bulk of WTe_2 induced by the Berry connection polarizability tensor[5]. Fig. S4 shows the third-order nonlinear Hall effect in device A at 1.8 K. The third-order nonlinear Hall effect shows angle-dependence following $\frac{V_H^{3\omega}}{(I^\omega)^3} \propto cos(\theta - \theta_0)sin(\theta - \theta_0)[(\chi_{22}r^4 - 3\chi_{12}r^2)sin^2(\theta - \theta_0) + (3\chi_{21}r^2 - \chi_{11})cos^2(\theta - \theta_0)]$ (Ref.[47]), where $V_H^{3\omega}$ is the third-harmonic Hall voltage, χ_{ij} are elements of the third-order susceptibility tensor. The fitting curve for this angle dependence is shown by the red line in Fig. S4c, which yields a similar misalignment angle θ_0 ~ 1.3°.

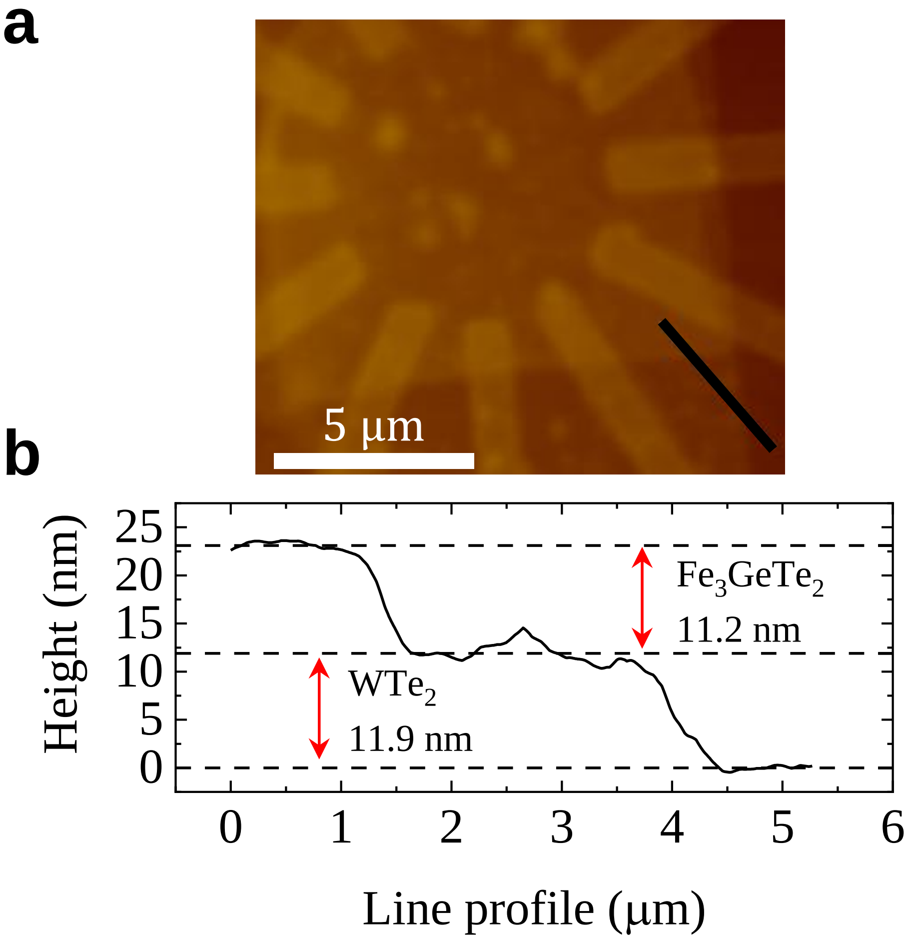

Fig. S1 | The atomic force microscope image of device A. The line profile shows the thickness of the WTe_2 is 11.9 nm, corresponding to 17-layer thickness. The thickness of the Fe_3GeTe_2 is 11.2 nm, corresponding to 14-layer thickness.

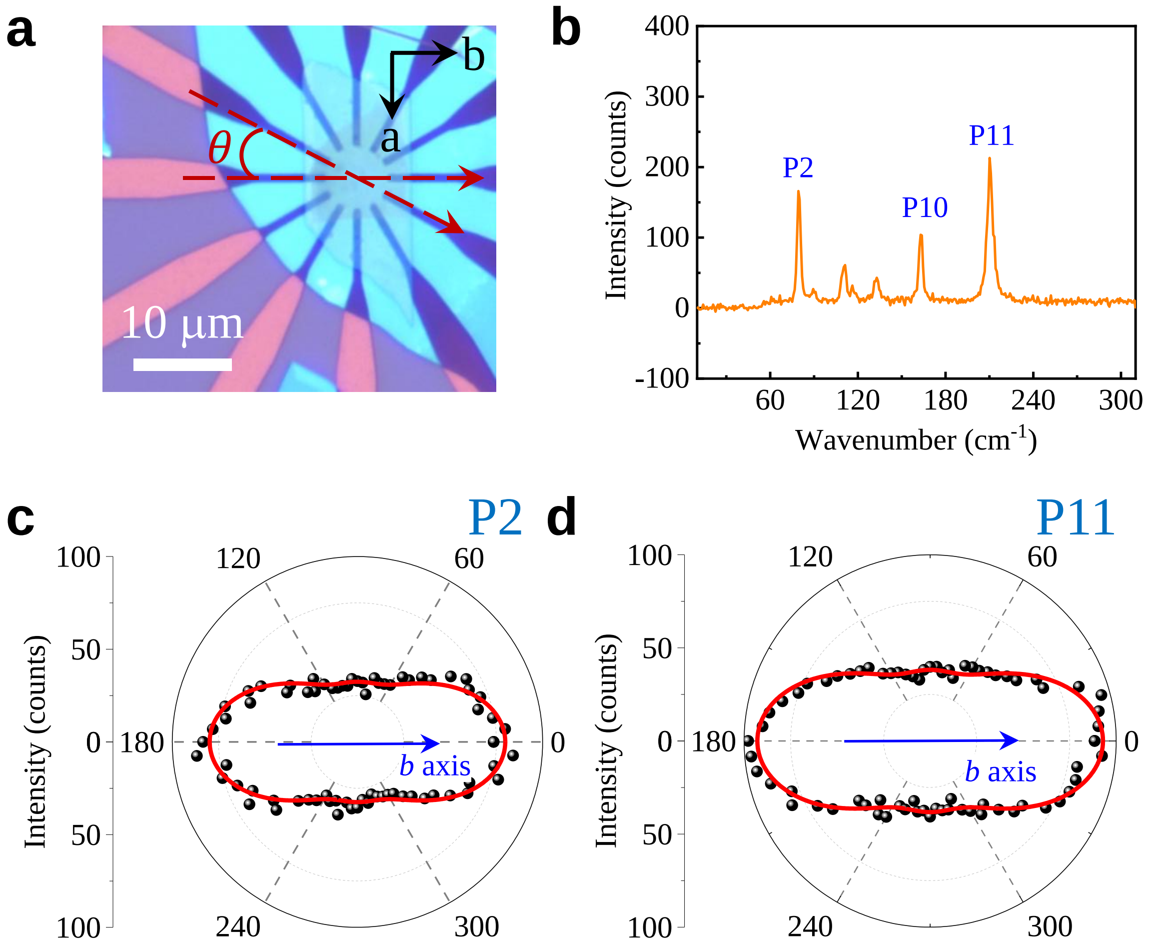

Fig. S2 │ Polarized Raman spectroscopy of few-layer WTe_2 to determine the crystalline orientation. a, The optical image of device A. **b,** A typical Raman spectrum of device A, where the polarization direction is approximately along *b* axis. **c,d,** Polarization dependence of intensities of peaks (**c**) P2 and (**d**) P11 for device A.

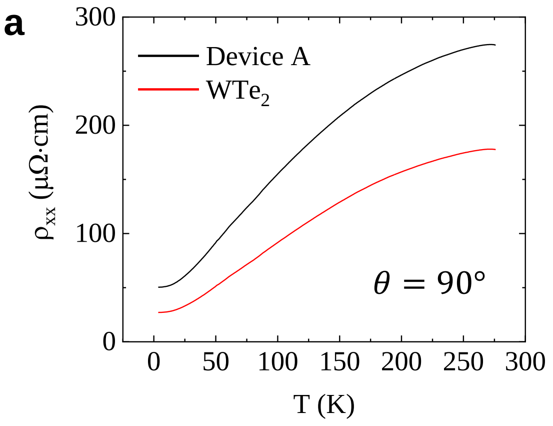

Fig. S3 | Basic transport properties of device A. a, The resistivity as a function of temperature. **b,** Magnetoresistance (MR) and Hall resistance as a function of magnetic field at 1.8 K, marked by black and red, respectively. The MR is defined as $\frac{R_{xx}(\mu_0 H)-R_{xx}(0)}{R_{xx}(0)} \times 100\%$. The large non-saturated MR and Hall resistance demonstrate two-carrier transport characteristics, indicating a nearly compensated electron and hole density in WTe_2.

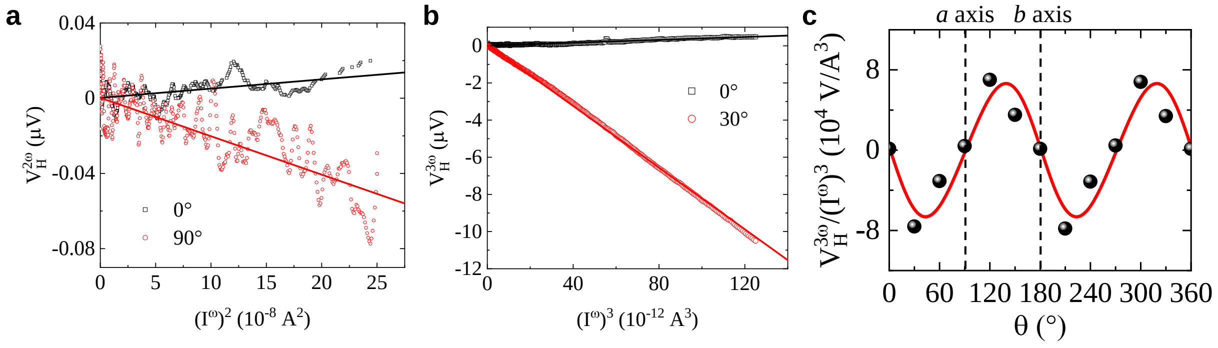

Fig. S4 | Higher-order nonlinear Hall effect in device A at 1.8 K. a, The second-order nonlinear Hall voltage as a function of $(I^\omega)^2$, where I^ω along $\theta = 0°$ and 90° is marked by black and red, respectively. **b,** The third-order nonlinear Hall voltage as a function of $(I^\omega)^3$, where I^ω along $\theta = 0°$ and 30° is marked by black and red, respectively. **c,** The angle dependence of the third-order nonlinear Hall effect.

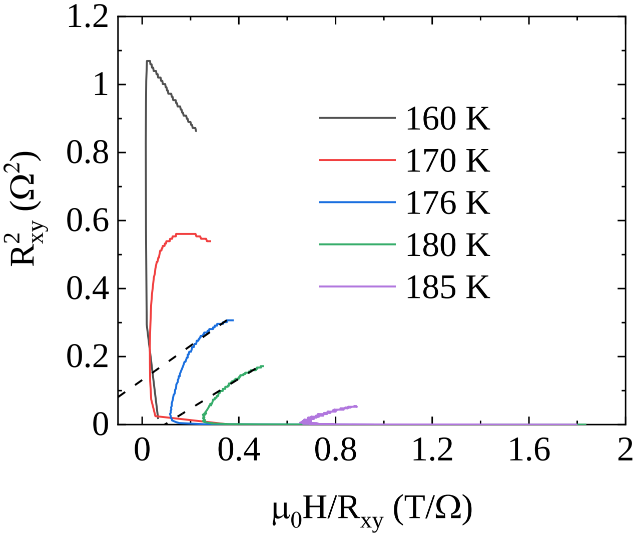

Fig. S5 | Arrott plot of device A. The Curie temperature ~180 K is estimated.

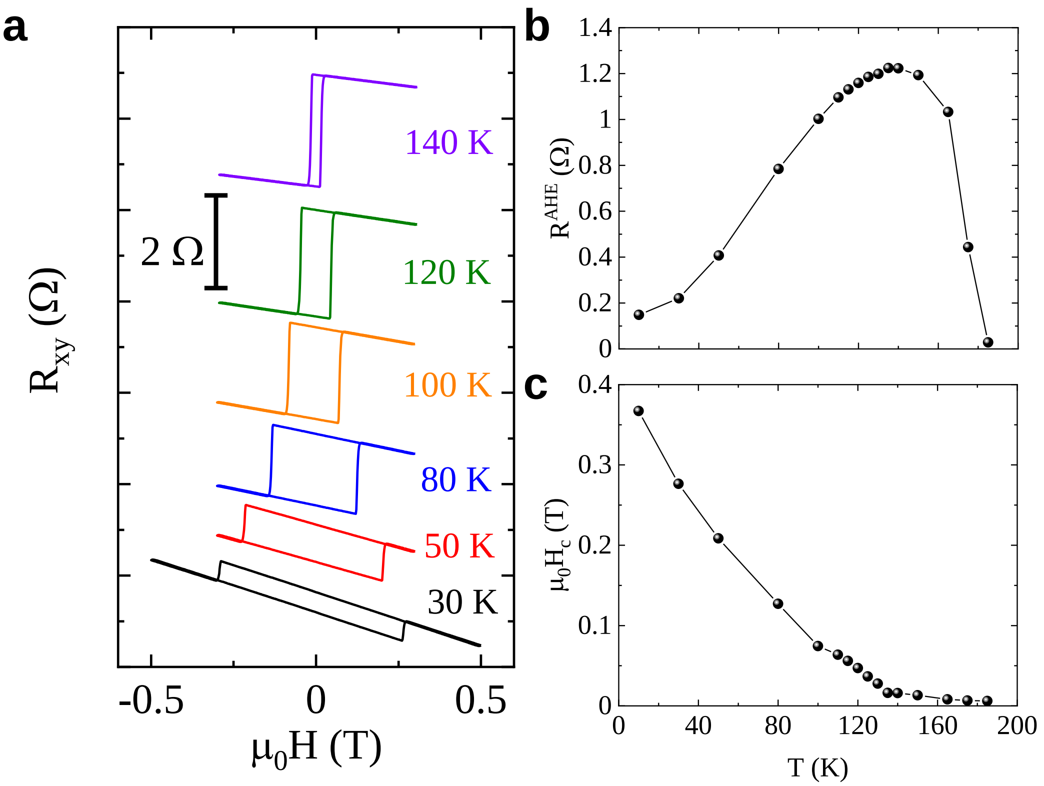

Fig. S6 | Magnetic properties of device A. a, The Hall resistance as a function of magnetic field at various temperatures. **b,** The anomalous Hall resistance, defined as the half of the R-H loop height, as a function of temperature. **c,** The coercive field as a function of temperature.

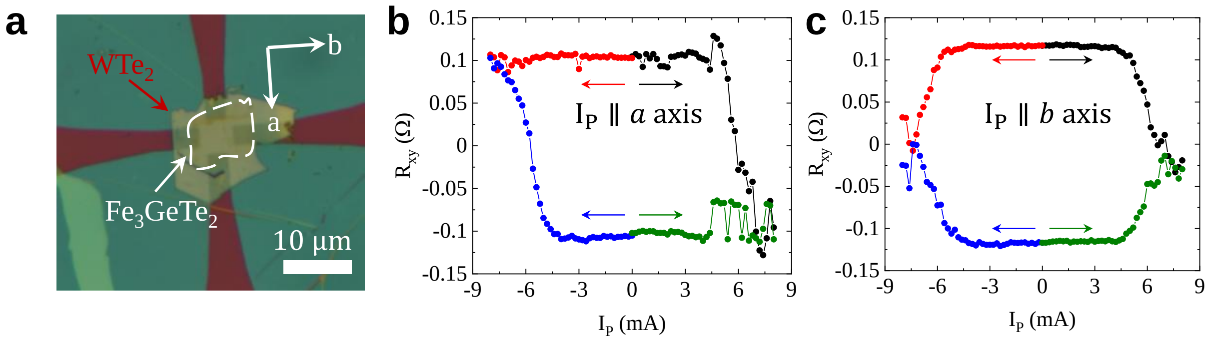

Fig. S7│Reproducible results in device B. a, The optical image of device B. **b, c,** Hall resistance as a function of pulse current I_P at 120 K for I_P approximately along *a* axis and *b* axis, respectively. Before sweeping I_P from zero to large positive or negative values, the magnetization state is initialized by perpendicular magnetic field.

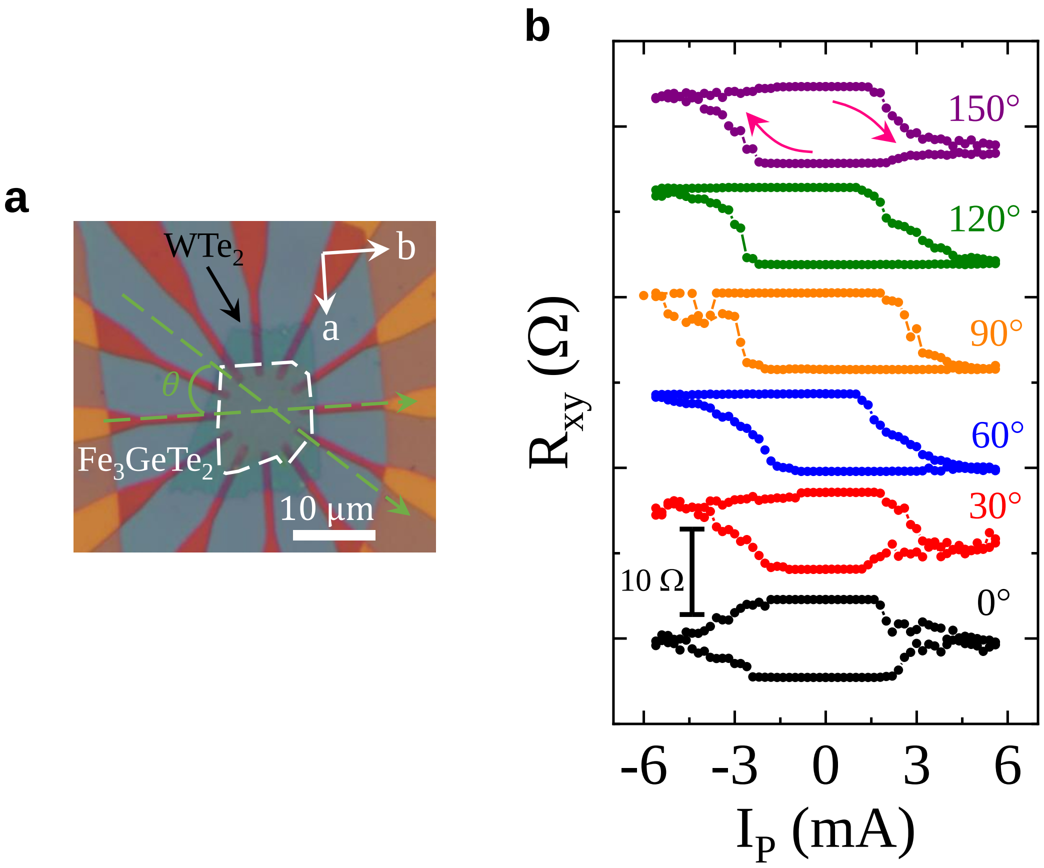

Fig. S8│Reproducible results in device C. a, The optical image of device C. **b,** The R_{xy}-I_P loops at 120 K with I_P applied along different angle θ. Before sweeping I_P from zero to large positive or negative values, the magnetization state is initialized by perpendicular magnetic field. The curves are shifted for clarity.

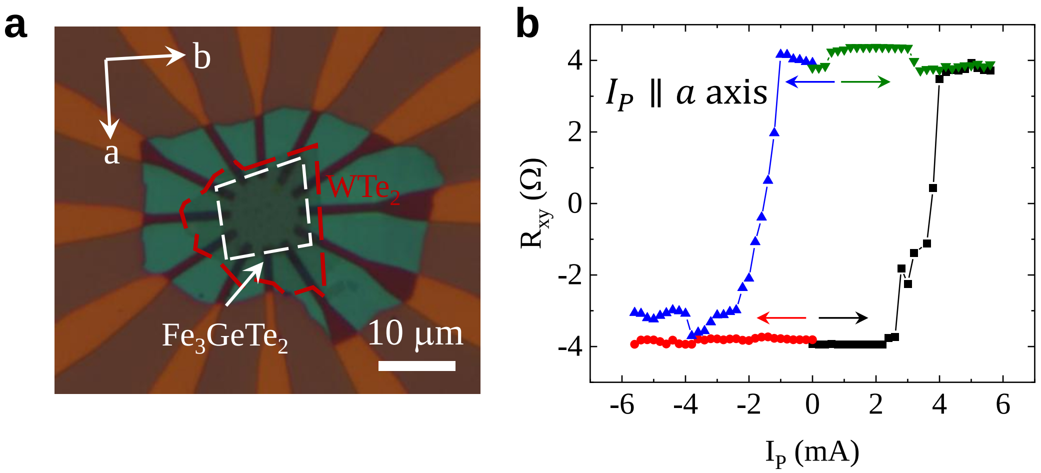

Fig. S9 | Reproducible results in device D. a, The optical image of device D. **b,** Hall resistance as a function of pulse current I$_P$ at 120 K. I$_P$ is applied approximately along *a* axis. Before sweeping I$_P$ from zero to large positive or negative values, the magnetization state is initialized by applying perpendicular magnetic field.

Table S1| Summary of the thickness of WTe$_2$ (t_{WTe_2}) and Fe$_3$GeTe$_2$ (t_{FGT}), and the switching current density J_c at 120 K along *a* axis in different devices.

Device	t_{WTe_2} (nm)	t_{FGT} (nm)	J_c $(10^{10}\ A/m^2)$
A	11.9	11.2	8.5
B	14.7	12	8.6
C	5.6	14.4	6.5
D	3.5	12	8.4

References

[1] Wang L, Meric I, Huang P Y, Gao Q, Gao Y, Tran H, Taniguchi T, Watanabe K, Campos L M, Muller D A, Guo J, Kim P, Hone J, Shepard K L and Dean C R. One-Dimensional Electrical Contact to a Two-Dimensional Material. *Science* **342** 614-617 (2013).

[2] Kim M, Han S, Kim J H, Lee J U, Lee Z and Cheong H. Determination of the thickness and orientation of few-layer tungsten ditelluride using polarized Raman spectroscopy. *2D Mater.* **3** 034004 (2016).

[3] Fei Z, Huang B, Malinowski P, Wang W, Song T, Sanchez J, Yao W, Xiao D, Zhu X, May A F, Wu W, Cobden D H, Chu J H and Xu X. Two-dimensional itinerant ferromagnetism in atomically thin Fe$_3$GeTe$_2$. *Nature Mater.* **17** 778–782 (2018).

[4] Fatemi V, Gibson Q D, Watanabe K, Taniguchi T, Cava R J and Jarillo-Herrero P Magnetoresistance and quantum oscillations of an electrostatically tuned semimetal-to-metal transition in ultrathin WTe$_2$. *Phys. Rev. B* **95** 041410 (2017).

[5] Lai S, Liu H, Zhang Z, Zhao J, Feng X, Wang N, Tang C, Liu Y, Novoselov K S, Yang S A and Gao W B. Third-order nonlinear Hall effect induced by the Berry-connection polarizability tensor. *Nat. Nanotechnol.* **16** 869–873 (2021).